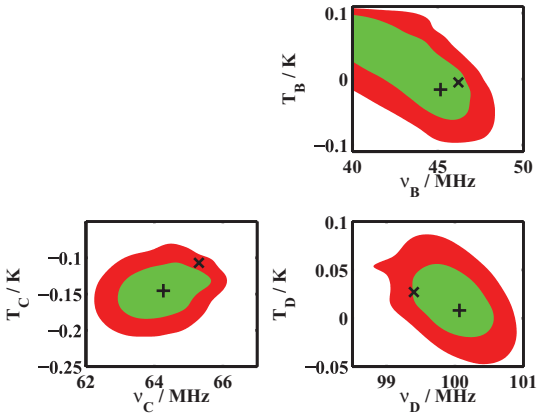

Figure 6. Confidence regions on turning points B, C and D of the cosmological signal, assuming a realistic instrument, and that we have no prior information on the parameters of the instrument model and the solar spectrum. Eight sky regions are observed for a total of 3000 h. Colours and symbols are as for Fig. 5, but for this and all subsequent figures the axis scales vary.

while those for the third lie just outside its border, suggesting that the parameters have been recovered without significant bias, even for the most difficult turning point at low frequency (turning point B). Further, the size of the confidence regions is small and, thus, very promising, allowing the three turning points to be distinguished clearly from one another.

5 RESULTS AND DISCUSSION

Having looked at signal recovery for a perfect instrument, we now move on to a more realistic case based on the simulated properties of the proposed *DARE* satellite. We start by assuming that there is no meaningful prior information on any of the parameters, so that they are constrained only by the satellite science data. The confidence regions for this case, for a single random noise realization assuming a total of 3000 h of integration time (375 h per sky area), are shown in Fig. 6. It is easy to see, noting the difference in axis scale between Figs 5 and 6, that the parameter constraints are significantly degraded. The frequency of turning point C, for example, is found with an error of around ±1 MHz, rather than ±0.5 MHz from a perfect instrument. The best-fitting values of all the parameters are somewhat offset from the true values, but the error appears to be consistent with the confidence regions estimated from MCMC. Turning point B is worst affected: the 68 per cent confidence region spans a range of well over 100 mK in temperature, and extends in frequency to below the bottom end of the range (40 MHz), where we have truncated the scale of the plot. The constraint on its frequency is therefore very model-dependent, and is probably best viewed as an upper limit, ruling out a turning point above ∼48 MHz with 95 per cent confidence (this upper limit is properly computed from the fully marginalized, one-dimensional probability distribution of ν_B; see Table 1).

The temperature of the other turning points is not as well determined as their frequency, in the sense of how constraining the limits would be for models of the dark ages, but some measurements are still obtained. For all three turning points, the temperature is slightly underestimated. This is simply because the temperature errors are correlated across the band rather than because of some bias in the method: we examine the correlations further in Section 5.1. The correlation arises because of the difficulty of measuring the overall normalization of the signal (as opposed to its spectral variation) in the presence of the strong foregrounds.

Even though the parameter constraints may look weak compared to the case for the perfect instrument of Fig. 5, the foreground parameters are very well constrained. For example, the spectral index in one of the sky regions at 80 MHz is found to be $-2.350\,898 \pm 0.000\,042$ (2σ errors), compared to a true value of $-2.350\,903$. This illustrates the dynamic range required for such an experiment. The Sun, being a weaker source, does not have its spectral index determined quite so well: we find a value of 1.991 ± 0.011 at 80 MHz, with the true value being 1.989.

Fig. 7 shows how the constraints are improved if we impose tight, Gaussian priors on the parameters of the non-diffuse foregrounds and the instrument, again assuming 3000 h of observation. $T_0^{i,\mathrm{Sun}}$ is assumed to be known to 0.1 per cent for all i, as are the temperature and reflectivity of the Moon, while $\{a_1^{\mathrm{Sun}}, a_2^{\mathrm{Sun}}, a_3^{\mathrm{Sun}}\}$ are known with an error of ±0.001. The coefficients of $\Gamma(\nu)$ are known to one part in 10^6 (i.e. almost perfectly), while T_{rcv} and ϵ are known to 0.1 per cent. The assumption that the reflection coefficient is known to one part in 10^6 is well beyond typical expectations at present, and is thus an optimistic prior. Most antennas are characterized at the 1 per cent level today, but devices designed to make accurate impedance measurements are stated in their specifications to perform to an accuracy of <0.1 per cent, and it is reasonable that this

Table 1. 95 per cent confidence intervals (or, in some cases, upper and lower limits) on the frequency, redshift and temperature of turning points B, C and D for the various sets of assumptions we have considered. The first column gives a brief description of each simulation, while the second shows which figures were plotted using data from that simulation. The remaining columns show the constraints. The first row shows the true input values of the parameters, for comparison. All simulations assume 3000 h of observation, unless otherwise stated. A fuller description of each model is given in the relevant figure captions.

		Turning point B			Turning point C			Turning point D		
Description	Figures	ν/MHz	z	T/mK	ν/MHz	z	T/mK	ν/MHz	z	T/mK
True input values	–	46.2	29.7	−5	65.3	20.8	−107	99.4	13.29	27
Perfect instrument	5	$46.6^{+0.9}_{-1.1}$	$29.5^{+0.7}_{-0.6}$	-10^{+22}_{-22}	$65.3^{+0.7}_{-0.6}$	$20.7^{+0.3}_{-0.2}$	-111^{+11}_{-11}	$99.3^{+0.3}_{-0.2}$	$13.30^{+0.03}_{-0.03}$	23^{+9}_{-12}
No prior information	6,14	<47.6	>28.8	55^{+45}_{-112}	$64.3^{+1.3}_{-1.6}$	$21.1^{+0.6}_{-0.5}$	-141^{+43}_{-55}	$100.0^{+0.7}_{-0.8}$	$13.21^{+0.11}_{-0.10}$	8^{+61}_{-41}
All tight priors	7,8,9	$45.6^{+2.4}_{-5.2}$	$30.1^{+4.1}_{-1.5}$	-7^{+84}_{-42}	$65.0^{+0.8}_{-0.9}$	$20.9^{+0.3}_{-0.3}$	-116^{+18}_{-17}	$99.5^{+0.4}_{-0.3}$	$13.27^{+0.05}_{-0.05}$	23^{+17}_{-15}
Tight inst. priors	10	$42.6^{+4.8}_{-3.1}$	$32.3^{+2.7}_{-2.3}$	95^{+6}_{-111}	$65.3^{+0.7}_{-0.8}$	$20.7^{+0.3}_{-0.2}$	-102^{+18}_{-17}	$99.1^{+0.4}_{-0.3}$	$13.33^{+0.05}_{-0.05}$	32^{+18}_{-14}
Tight non-inst. priors	11	<49.0	>28.0	25^{+75}_{-65}	$64.7^{+1.3}_{-1.6}$	$21.0^{+0.5}_{-0.4}$	-94^{+34}_{-52}	$99.6^{+1.0}_{-0.8}$	$13.26^{+0.11}_{-0.13}$	51^{+35}_{-48}
1000 h integration	12	<48.9	>28.1	-11^{+108}_{-51}	$65.0^{+1.1}_{-1.5}$	$20.9^{+0.4}_{-0.4}$	-125^{+26}_{-24}	$99.6^{+0.5}_{-0.4}$	$13.26^{+0.07}_{-0.08}$	17^{+24}_{-22}
10000 h integration	13	$46.9^{+1.5}_{-4.4}$	$29.3^{+3.2}_{-1.0}$	-9^{+71}_{-22}	$65.4^{+0.7}_{-0.5}$	$20.7^{+0.2}_{-0.2}$	-98^{+16}_{-11}	$99.4^{+0.2}_{-0.3}$	$13.30^{+0.03}_{-0.03}$	35^{+11}_{-11}

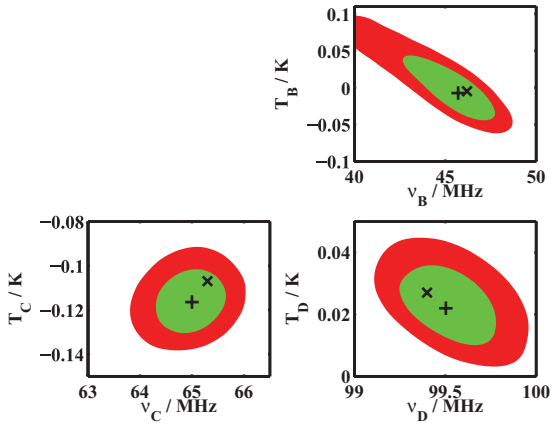

Figure 7. Confidence regions on turning points B, C and D of the cosmological signal, assuming a realistic instrument observing eight sky regions for a total of 3000 h, but with tight priors on the parameters of the instrument model, the solar spectrum and the properties of the Moon. We assume here, as throughout, that there is no prior information on the parameters of the diffuse foregrounds or the 21-cm signal itself. Colours and symbols are as for Fig. 5.

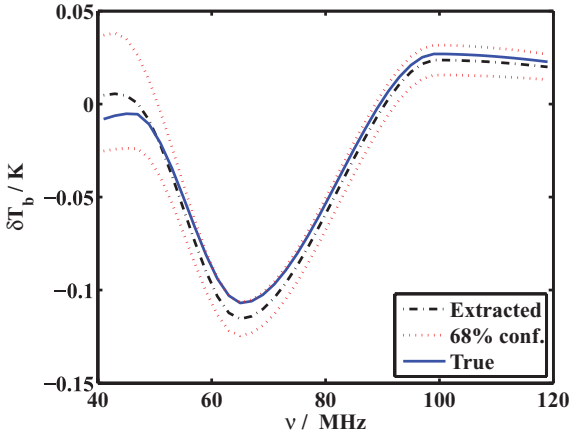

Figure 8. The mean extracted signal (dot–dashed black line) and 68 per cent confidence limits on this mean (dashed red lines) are compared to the 'true' signal constructed from the input parameters to the simulation (solid blue line). This plot assumes an instrument observing eight areas of the sky for a total of 3000 h, with tight priors on the parameters concerning the instrument, the Sun and the Moon, as in Fig. 7.

level could be achieved. This topic is being actively worked on with EDGES, the closest current analogue to *DARE*, in the field and the laboratory, with a target of achieving an accuracy of one part in 10^4. Furthermore, it should be possible to treat the unknown aspects of the reflection coefficient with more physically motivated models than the DCT, which would help to reduce the effective degrees of freedom and so approach the desired accuracy. Our priors on $T_{\rm rcv}$ and ϵ are more plausible, and they could well be measured in the lab to this level before launch.

Under these conditions, the parameter constraints approach more closely those for the perfect instrument of Fig. 5. The main exception is that it becomes harder to rule out turning point B lying at a much lower frequency and higher temperature. A good measurement can only be found at 68 per cent confidence. The 95 per cent confidence region extends outside the band for which we have data, and any inferences about the properties of the signal in that region depend strongly on the assumed signal model. The shape of the confidence region suggests that our data actually tell us the amplitude and slope of the signal at low frequency, and that turning point B lies somewhere on a curve consistent with that amplitude and slope within the errors.

Since the instrumental frequency response and the non-diffuse foregrounds are well known, the weak constraint on turning point B compared to the perfect instrument must occur because of the reduced sensitivity at low frequencies, caused by the large value of $|\Gamma(\nu)|$ there. To find the position of turning point B precisely, it may be necessary to have an instrument with better sensitivity at low frequency, and possibly a lower minimum frequency. This is difficult to achieve (see the steep drop in sensitivity at low frequencies in Fig. 4), though one possible route would be a larger antenna and ground screen, which may be awkward and expensive for a satellite mission. Even then, it is hard to design an antenna which can cover a frequency range which is more than a factor of $\sim$3 without (for example) the antenna changing mode at the top end of the frequency range and introducing frequency structure into the response. The large uncertainty in current theoretical models of the signal means that an instrument with a range of, say, 35–105 MHz would run the risk of missing out entirely on turning point D, which we would otherwise hope to constrain quite precisely. Fig. 7 suggests we are close enough to a measurement of turning point B that this may be possible with some smaller tweak to the design without having to change the current *DARE* frequency range.

We show how the parameter constraints of Fig. 7 translate into constraints on the shape of the 21-cm signal in Fig. 8. Here we plot the true signal, the mean over all the samples of the extracted signal at each frequency, and a 68 per cent confidence interval around this mean. The shape of the signal is recovered quite well, but the frequency of the turning points seems, visually, to be recovered more accurately than the temperature. The absolute normalization of the curve is difficult to determine.

The width of the error bars is larger at the lower end of the frequency range than at the upper end, but not to the extent that would be expected if one were simply to use the rms thermal noise at each frequency to determine the error bar, since the sky temperature in the lowest frequency channel is >10 times that in the highest frequency channel, and this is the most important contributor to the thermal noise. Instead, the errors across the whole band are highly correlated, since the shape of the signal is reconstructed only from the six parameters giving the position of the turning points.

Before moving on from the case where we have good prior information on the properties of the Sun, the Moon and the instrument, we illustrate the errors on individual parameters which can be achieved in this case by showing the marginalized distributions of a subset of them in Fig. 9. It is also reassuring to be able to check that the distributions seem fairly smooth and well behaved. Complicated, multimodal distributions (or, for example, strongly curving degeneracies between different parameters) would be awkward for the sampler we have implemented here, and might require a more sophisticated method to sample them efficiently.

We now wish to consider whether the improvement between Figs 6 and 7 comes from our better knowledge of the non-diffuse foregrounds (in particular the Sun) or of the instrument. To this end, in Fig. 10 we show results obtained using the tight priors on $\Gamma(\nu)$ given above, but reverting to weak priors on the spectral parameters of the Sun.

The results for turning points C and D are almost as good as for the previous case, showing that superb knowledge of the instrument is the most important factor in extracting the 21-cm signal

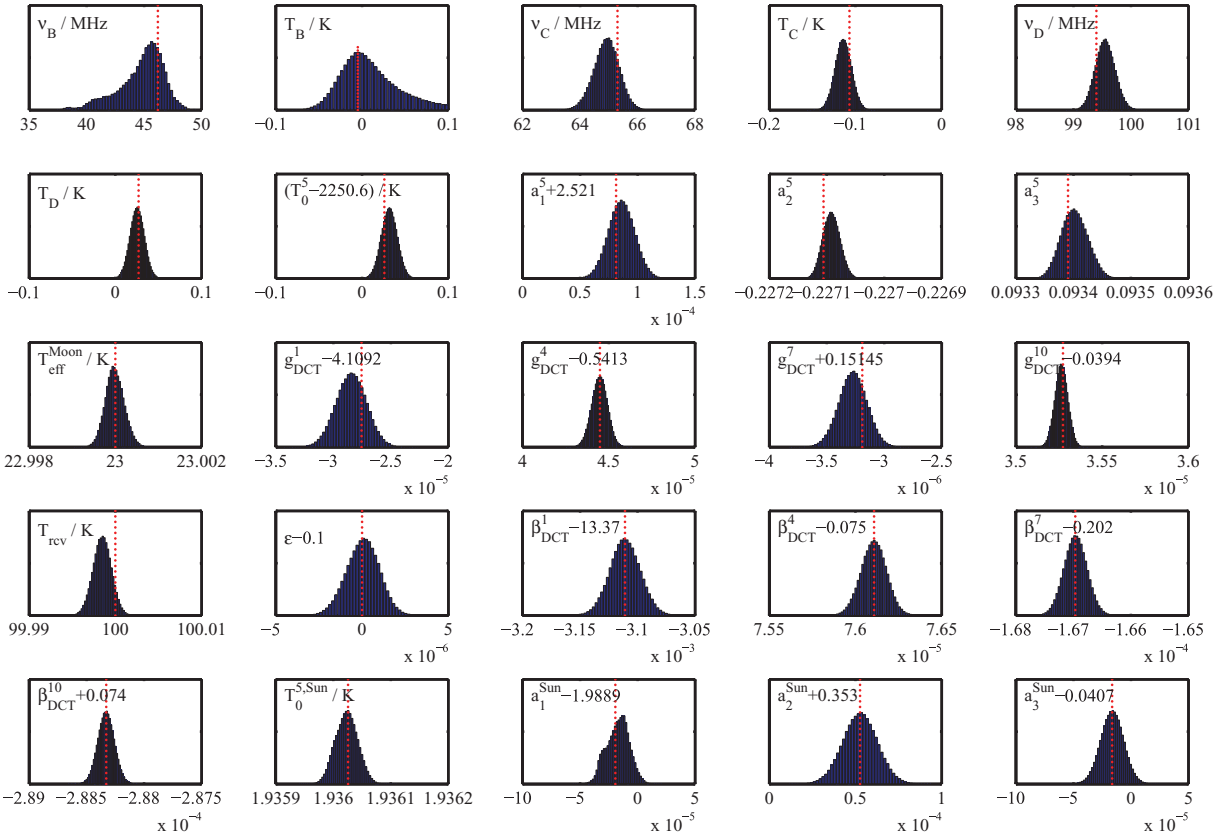

Figure 9. One-dimensional marginalized distributions of the parameters for the case when we have tight priors on the properties of the instrument, the Sun and the Moon, as in Figs 7 and 8. The vertical, red, dashed line shows the input value of the parameter. The names of the parameters given in each panel are as in the text, except that the DCT coefficients of $|\Gamma|$ and β are labelled $g^i_{\rm DCT}$ and $\beta^i_{\rm DCT}$, respectively.

accurately, though constraints on turning point B are notably degraded. Foreground parameters are also measured more precisely than for the case of Fig. 6: for example, the error on the spectral index of the Sun at 80 MHz is reduced by a factor of about 6. If the instrumental calibration can be improved by using the spectra at full time and frequency resolution, or by introducing extra mechanisms for internal calibration, then this would clearly be very desirable, and should be the subject of further study.

By contrast with Fig. 10, Fig. 11 shows the confidence regions we derive when we assume tight priors on the spectrum of the Sun (obtained perhaps by ground-based observations), but relax the priors on the coefficients of the instrumental response to their original size. The constraints on the signal parameters are improved only a little over those of Fig. 6, with the overall temperature normalization being especially hard to recover. None the less, external constraints on the solar spectrum would be valuable as a consistency check.

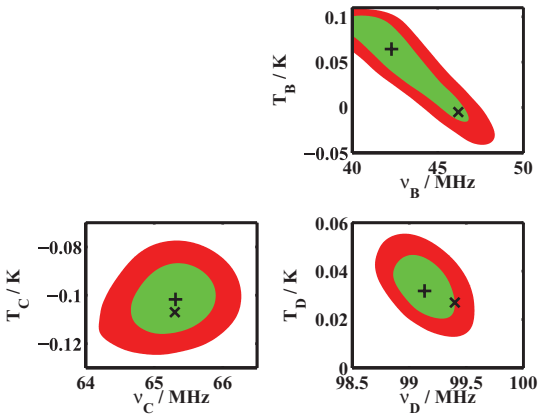

Figure 10. Confidence regions on turning points B, C and D of the cosmological signal, assuming a realistic instrument observing eight sky regions for a total of 3000 h, but with tight priors on the parameters of the instrument model. Colours and symbols are as for Fig. 5.

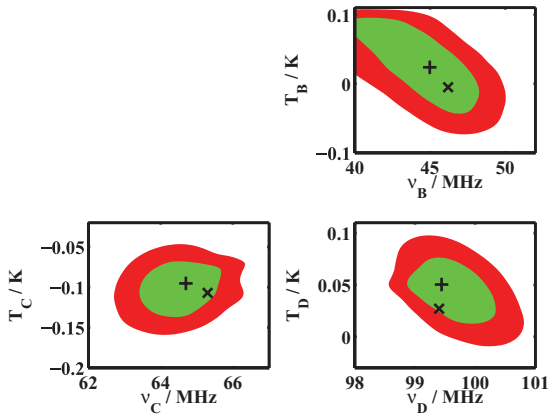

Figure 11. Confidence regions on turning points B, C and D of the cosmological signal, assuming a realistic instrument observing eight sky regions for a total of 3000 h, and with tight priors on the parameters of the solar spectrum and the Moon. Colours and symbols are as for Fig. 5.

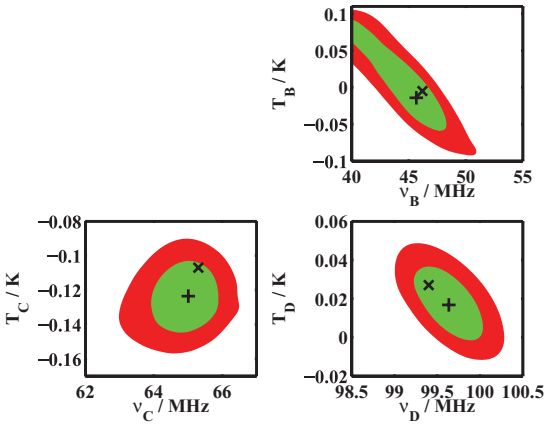

Figure 12. Confidence regions on turning points B, C and D of the cosmological signal, assuming a realistic instrument observing eight sky regions for a total of 1000 h, and with tight priors on the parameters of the instrument model, the solar spectrum and the Moon. Colours and symbols are as for Fig. 5. This figure should be compared to Fig. 7, which makes the same assumptions and differs only in the amount of integration time.

Finally, we look at the effect of changing the available integration time. Results so far have used 3000 h of data; for Fig. 12 we assume instead only 1000 h of data, as may occur if the satellite is able to observe for only one year. Otherwise, the assumptions are the same as for Fig. 7, i.e. tight priors on both the instrument and the non-diffuse foregrounds are assumed.

The effect is as one might expect, with confidence regions on the parameters being enlarged somewhat. Turning points C and D can still be localized: a single year of data from our reference experiment could yield a detection of the first astrophysical sources of heating in the Universe, and the start of the EoR. It becomes impossible to obtain anything other than an upper limit on the frequency of turning point B, however: the sensitivity at the low frequencies is simply not sufficient for a clear measurement of its position.

To make sure that a realistic instrument can find a firm, 2σ detection of the frequency of turning point B given sufficient integration time, we show results for 10 000 h of observation in Fig. 13. In this case, the 2σ contours do indeed close above 40 MHz, though there

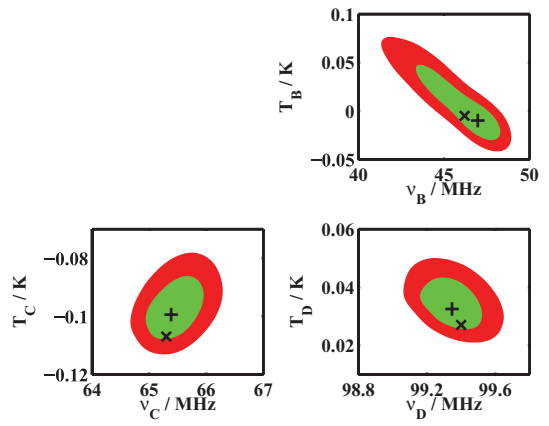

Figure 13. Confidence regions on turning points B, C and D of the cosmological signal, assuming a realistic instrument observing eight sky regions for a total of 10000 h, and with tight priors on the parameters of the instrument model, the solar spectrum and the Moon. Colours and symbols are as for Fig. 5. This figure should be compared to Figs 7 and 12, which make the same assumptions and differ only in the amount of integration time.

is still a significant degeneracy between the frequency and temperature of turning point B. The positions of turning points C and D are measured with improved accuracy compared to our baseline case, though further study of such deep integrations may need the possible systematics to be considered more carefully. An integration of this length would be challenging from space, needing either a mission of long duration or a very high observing efficiency (possibly both). It is likely that the requisite noise level in the vicinity of turning point B can be achieved more easily by modifications to the design of the spacecraft or radiometer system. Better constraints on turning point B might also come by extending the frequency coverage to lower frequencies.

We summarize the constraints on the parameters of the signal for all the different assumptions we have considered in Table 1. Here, we show 95 per cent confidence intervals (or, in some cases, upper or lower limits) on the frequency, redshift and temperature of the turning points, and record the figures for which each set of assumptions was used.

5.1 Correlation between parameters

The contour plots we have shown allow one to see clearly if the inferred frequency and temperature of a given turning point are correlated, or in other words if there is a degeneracy between these two parameters. The frequency, $\nu_{\rm B}$, and temperature, $T_{\rm B}$, of turning point B, for example, are clearly anticorrelated in all our figures. Such correlations may exist between all our parameters, and allow one to pick out possible degeneracies. Therefore, in Fig. 14, we show a scaled version of the covariance matrix of the parameters, such that a value of 1 (-1) in pixel $\{i, j\}$ indicates that the value of parameters i and j in the MCMC samples is perfectly (anti)correlated, with a

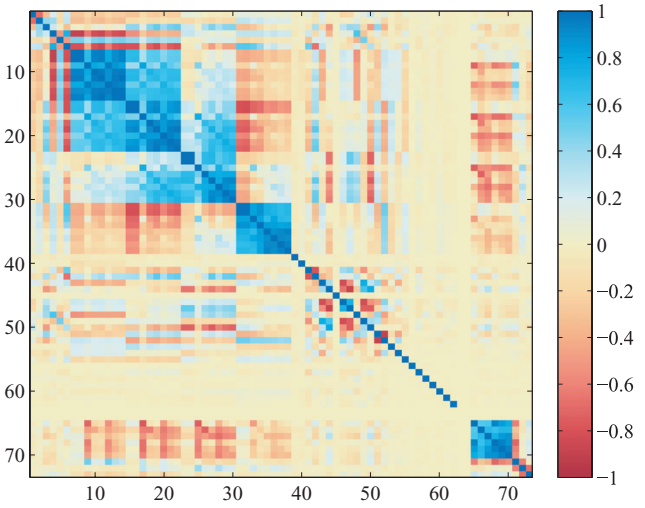

Figure 14. The scaled covariance matrix of all the parameters of the model, for a realistic instrument and assuming no meaningful prior information on the parameter values, as for Fig. 6. By the 'scaled' covariance matrix, we mean that each pixel shows the correlation coefficient between two parameters, where a value of zero implies no correlation, and a value of 1 (-1) means perfect (anti)correlation. The 1s on the diagonal come about because each variable is perfectly correlated with itself. The order of the parameters is given in Table 2. Note that parameters 63 ($T_0^{1,\rm Sun}$) and 64 ($T_0^{2,\rm Sun}$) are set to be identically zero since the Sun is assumed to be occluded by the Moon in sky regions 1 and 2, which accounts for the obvious stripe at this position. This figure is best viewed in colour, to make the difference between correlations (blue) and anticorrelations (red) more clear.

Table 2. Numbering of the rows of the scaled covariance matrix in Fig. 14

Row/column number	Parameter description
1–2	Frequency and temperature of turning point B
3–4	Frequency and temperature of turning point C
5–6	Frequency and temperature of turning point D
7–14	T_0^i, $i = 1, \ldots, 8$
15–22	a_1^i, $i = 1, \ldots, 8$
23–30	a_2^i, $i = 1, \ldots, 8$
31–38	a_3^i, $i = 1, \ldots, 8$
39	Effective temperature of the Moon
40	Reflectivity of the Moon
41–50	DCT coefficients of $\|\Gamma(\nu)\|$
51–52	$T_{\rm rcv}$ and ϵ
53–62	DCT coefficients of $\beta(\nu)$
63–70	$T_0^{i,\rm Sun}$, $i = 1, \ldots, 8$
71–73	$a_1^{\rm Sun}$, $a_2^{\rm Sun}$ and $a_3^{\rm Sun}$

value of zero indicating no correlation. The key to the numbering of the rows and columns of the image is given in Table 2.

As expected, parameters 1 and 2 ($\nu_{\rm B}$ and $T_{\rm B}$) are easily seen to be anticorrelated, with the correlation coefficient between them here being −0.69. Other strong correlations are clearly apparent. For example, the block structure near the diagonal comes about because the parameters within one group, such as the normalization of the foreground temperatures in the different regions, T_0^i, are strongly correlated with each other. When a parameter outside this group is varied, the foregrounds in each region will all have to change in a similar way to compensate, introducing a correlation.

Some of the other features of the covariance matrix are straightforward to understand. For example, the temperatures of turning points C and D are strongly anticorrelated with the foreground temperature, T_0^i, for all i: an overall increase in the brightness temperature of the 21-cm signal can be compensated for by a decrease in the brightness of the foregrounds in every region of the sky. This very strong anticorrelation may help to explain why the inferred temperatures of the turning points become positively correlated with each other, an effect which is evident in many of our figures. It is more difficult to find 'interesting' constraints on the temperatures of the turning points than on the frequencies. The similar temperature offsets of the different turning points for any given noise realization may, however, allow us to recover the overall shape of the signal well, even if its absolute normalization is uncertain. The anticorrelation between the temperature of turning point B and the foreground temperature is less strong than for the other turning points, but this is mainly because of the larger statistical error on the temperature of turning point B.

The difficulty of pinning down the overall normalization of the 21-cm signal might be mitigated somewhat if we could fix its temperature at some frequency using external or theoretical constraints. To some extent we do this already by fixing the positions of turning points A and E, which lie outside the observed band, and this appears to be insufficient. The best candidate for a normalizing point inside the *DARE* band is probably turning point D: looking at equation (1), if $x_{\rm H\,I} \approx 1$ (reionization not yet seriously under way) and $T_{\rm S} \gg T_\gamma$ (heating has saturated), the other terms can be computed from well-constrained cosmological parameters and could be assumed to be known. Interferometric experiments may be able to shed some light on the value of $x_{\rm H\,I}$ and $T_{\rm S}$ and hence provide a normalization indirectly. An EDGES-like experiment might also span both the frequency of turning point D and high frequencies at which $x_{\rm H\,I} \ll 1$ so the signal is known. It would face similar problems to our reference experiment in constraining the large-scale spectral shape, however, and so it is not clear it could provide a much better temperature for turning point D.

Some features of the correlation matrix are more subtle: for example, there is a striking anticorrelation between the normalization of the solar spectrum in the different sky regions, $T_0^{i,\rm Sun}$, and the running of the spectral index of the diffuse foregrounds, a_2^i. This appears to come about because of the inverted spectrum of the Sun relative to the spectrum of the diffuse foregrounds: increasing $T_0^{\rm Sun}$ has a larger relative effect at high frequency, where the diffuse foregrounds are weaker, and so the spectrum of the diffuse foregrounds is made steeper at high frequencies to compensate.

Including the effect of the Sun also impacts the correlation structure of the other foreground parameters. In this simulation, we assumed that the contribution of the Sun to sky areas 1 and 2 (rows 63 and 64) was identically zero, because these areas were observed while the Sun was occluded by the Moon. This leads to the obvious stripe at this position in the correlation matrix. One can easily see that the correlations between the parameters of the diffuse foregrounds in areas 1 and 2 are stronger than for the other sky areas: they have less freedom to vary independently when there is no solar contribution to take up the slack. This feature, and the anticorrelation between a_2^i and $T_0^{i,\rm Sun}$, justifies our assertion in Section 3.3 that it is important to include the effect of the Sun in the modelling.

Degeneracies between the instrumental parameters other than $\beta(\nu)$ (rows 41–53) appear to be very complex. This may be an artefact of our parametrization of $\Gamma(\nu)$ in terms of DCT coefficients, though it is hard to know in the absence of a more physically motivated parametrization. Our main results assume tighter priors on these parameters than were used to make Fig. 14, which would make their correlations with the foreground and signal parameters less important. Although beyond the scope of this paper, it is possible that some alternative instrument design would produce smaller degeneracies between instrument and signal parameters, so that this sort of correlation analysis might help in optimizing the instrument design. This could be quite dependent on the signal model and parametrization though, and at present it seems better to concentrate on producing a smooth instrument response that can be described by a small number of parameters.

5.2 Comparison to other work

In this paper, we have made use of an MCMC approach to estimate constraints on the 21-cm global signal. There has been a certain amount of previous work making use of the Fisher matrix approximations to the likelihood, in the restricted case that the experiment genuinely sees the full sky. The initial work by Sethi (2005) in this area assumed that foregrounds could be removed separately and completely and so led to very optimistic predictions for cosmological constraints. More in line with our approach here, Pritchard & Loeb (2010) accounted for the need to simultaneously fit the foregrounds and the signal and introduced the turning point parametrization that we have used throughout this paper. Most recently, Morandi & Barkana (2011) investigated constraints on more general models of reionization.

The confidence regions obtained using strong priors on the instrumental and non-diffuse foreground parameters, and assuming 3000 h of data collection, are comparable to those found by Pritchard & Loeb (2010) for a 500 h observation of a single sky area (their

fig. 11). Fitting a model with many more parameters, as we do here, clearly degrades the constraints we can obtain on the parameters of interest for a given amount of integration time. Encouragingly, though, this comparison shows that the degradation is not catastrophic, and observing for a factor of a few longer allows us to recover the loss.

It would be desirable to compare to the larger body of work concentrating on probing the EoR with the global 21-cm signal (e.g. Morandi & Barkana 2011), using appropriate models for the frequency response (e.g. that of EDGES) and for the observational strategy, which is somewhat different for ground-based experiments. While our technique is applicable for models of the 21-cm signal other than the turning point parametrization used here, the signal during reionization is likely to be much more degenerate with the foregrounds and instrumental response than the turning point model. We defer a test of this statement to future work.

Probes of reionization other than the 21-cm line were studied by Pritchard, Loeb & Wyithe (2010), who discussed what current astrophysical priors can tell us about reionization. Their framework could easily be extended to account for global 21-cm experiments. Constraints from e.g. the CMB and the Lyα forest would not necessarily be applicable directly to the positions of the turning points in the parametrization we use here. Rather, constraints on the turning points from global 21-cm experiments could be transformed into constraints on the underlying physical model (the star formation history, the efficiency of X-ray production, etc.), and the other astrophysical constraints would also be applied in that space.

6 CONCLUSIONS

We have presented a model for the data from a proposed lunar-orbiting satellite to measure the global, redshifted 21-cm signal between 40 and 120 MHz. Fitting the parameters of this model to a realistic simulated data set using an MCMC algorithm yields constraints on the 21-cm signal that are comparable to those found using much simpler models for the foregrounds and instrument, despite the fact that we use the data to constrain $\approx$73 parameters, rather than 10. The key assumptions used in extracting the signal are that the foregrounds are smooth, that the instrumental response is also smooth and can be determined reasonably well by independent measurements, and that the 21-cm signal, averaged over the solid angle of our antenna beam, is constant across the sky while the foregrounds are not.

A mission of reasonable duration ($\sim$3 yr) can find the position of the bottom of the 'cosmic dawn' absorption trough in our fiducial model with an accuracy of around $\pm$1 MHz in frequency and $\pm$20 mK in temperature (2σ errors), provided that the instrumental response has been well characterized. The frequency position of the peak in emission at the onset of reionization can be found to within $\pm$0.5 MHz, while 'turning point B', marking the onset of Lyα pumping, can be determined with a 1σ error of around $\pm$2.5 MHz. For a shorter mission, of e.g. 1000 h, these constraints degrade somewhat, and it may only be possible to find an upper limit on the frequency of turning point B. A mission of 10000 h allows a good measurement of the frequency of turning point B, with a 2σ confidence interval that lies entirely within the *DARE* frequency band.

We have examined the effect of using prior information on the non-diffuse foregrounds, which may be amenable to measurement from the ground, and on the instrumental parameters. Priors on the foregrounds do not help a great deal, though clearly it will still be valuable to have independent, ground-based measurements of the foregrounds, to inform our modelling and to check that our measurements are consistent. Tightened priors on the instrument model, however, which correspond to improved calibration, reduce the statistical errors. They may also help to reduce the importance of temperature errors which are correlated across the frequency band, and which result in an uncertainty in the overall normalization of the 21-cm brightness temperature. Even if this correlation is present, it is likely that the shape of the 21-cm signal can be recovered accurately, since the absolute error on the temperature of each of the three turning points tends to be similar.

Interferometric experiments must also perform foreground subtraction, to an accuracy of around one part in 10^3 for the diffuse Galactic emission, and to one part in 10^6 or even 10^8 for bright point sources (Datta, Bowman & Carilli 2010). In this sense, arrays such as MWA, the Low Frequency Array and the Precision Array to Probe the Epoch of Reionization should characterize the properties of the Galactic and extragalactic foregrounds and validate the assumption that they can be modelled using functions which deviate little from power laws. They differ from experiments such as *DARE* or EDGES, however, in that they will use observations of specific point sources for calibration of gain and bandpass in a way that is not possible for sky-averaged experiments, since the latter cannot isolate the contribution to the measured spectrum from an individual source. For this reason, upcoming arrays have not been designed to achieve an intrinsically smooth bandpass that can be quantified with only a few parameters, and therefore will likely shed little light on the calibration or instrument modelling for sky-averaged experiments.

In this paper, we have focused on a particular reference experiment to illustrate our techniques. The methodology developed here is very general and can easily be extended to other global 21-cm experiments. As global 21-cm experiments continue to improve from their current relative infancy, there will be a need for improved techniques of statistical analysis. We have taken some early steps in that direction.

It is worth reiterating, however, that there are several other stages in the data analysis which must be passed before the methodology of this paper can be applied. Individual spectra taken with a short cadence (of e.g. 1 s) must be combined together using a map-making procedure to produce something like the eight independent spectra seen here. The frequency response must be internally calibrated, for example by toggling the receiver input between the antenna feeds and calibration loads. Narrow features such as RRLs or, in the case of ground-based experiments, RFI, must be excised. All these steps become more complicated for ground-based experiments. For the map making, an experiment fixed to the ground would not have the complete control over the pointing direction provided by a satellite, and would not have access to the whole sky. Moreover, the ionosphere effectively causes the sky seen by the antenna to vary with time. Internal calibration is made more awkward by changes in temperature and atmospheric conditions, while a space environment is more predictable. Finally, RFI is likely to be considerably more prevalent than RRLs. The main effects of these earlier steps on the MCMC method are likely to be the introduction of non-Gaussianity to the noise on the frequency spectra, and correlation between different sky areas, both of which affect the computation of the likelihood. It is not clear whether some of these effects could be captured with extra nuisance parameters in the MCMC. It will be important to study the preliminary analysis steps and their impact on the final extraction step in future

work, especially if our formalism is to be adapted for use with ground-based experiments.

ACKNOWLEDGMENTS

We thank Stuart Bale for providing an estimate of the noise caused by exospheric dust impacts on the antenna and the spacecraft. We also acknowledge the work of the *DARE* team in designing the mission, including Joseph Lazio, Rich Bradley, Chris Carilli, Steve Furlanetto, Avi Loeb, Larry Webster, Jill Bauman and Ian O'Dwyer. The authors are members of the LUNAR consortium (http://lunar.colorado.edu), headquartered at the University of Colorado, which is funded by the NASA Lunar Science Institute (via Cooperative Agreement NNA09DB30A) to investigate concepts for astrophysical observatories on the Moon.

REFERENCES

Bowman J. D., Rogers A. E. E., 2010, Nat, 468, 796
Bowman J. D., Rogers A. E. E., Hewitt J. N., 2008, ApJ, 676, 1
Burns J. O., 2009, in Heinz S., Wilcots E., eds, AIP Conf. Ser. Vol. 1201, The Monster's Fiery Breath: Feedback in Galaxies, Groups, and Clusters. Am. Inst. Phys., New York, p. 154
Burns J. O., Mendell W. W., eds, 1988, NASA Conf. Publ. 2489, Future Astronomical Observatories on the Moon
Burns J. O. et al., 2011, Advances Space Res., preprint (arXiv:1106.5194)
Ciardi B., Madau P., 2003, ApJ, 596, 1
Ciardi B., Salvaterra R., Di Matteo T., 2010, MNRAS, 401, 2635
Datta A., Bowman J. D., Carilli C. L., 2010, ApJ, 724, 526
Davis J. R., Rohlfs D. C., 1964, J. Geophys. Res., 69, 3257
de Oliveira-Costa A., Tegmark M., Gaensler B. M., Jonas J., Landecker T. L., Reich P., 2008, MNRAS, 388, 247
Field G. B., 1958, Proc. Inst. Radio Eng., 46, 240
Field G. B., 1959, ApJ, 129, 536
Furlanetto S. R., 2006, MNRAS, 371, 867
Furlanetto S. R., Oh S. P., Briggs F. H., 2006a, Phys. Rep., 433, 181
Furlanetto S. R., Oh S. P., Pierpaoli E., 2006b, Phys. Rev. D, 74, 103502
Gelman A., Rubin D. B., 1992, Statistical Sci., 7, 457
Gopalswamy N., Yashiro S., Akiyama S., Mäkelä P., Xie H., Kaiser M. L., Howard R. A., Bougeret J. L., 2008, Ann. Geophys., 26, 3033
Haario H., Saksman E., Tamminen J., 2001, Bernoulli, 7, 223
Hastings W. K., 1970, Biometrika, 57, 97
Jester S., Falcke H., 2009, New Astron. Rev., 53, 1
Keihm S. J., Langseth M. G., 1975, Icarus, 24, 211
Lewis A., Bridle S., 2002, Phys. Rev. D, 66, 103511
Liu A., Tegmark M., 2011a, Phys. Rev. D, 83, 103006
Liu A., Tegmark M., 2011b, preprint (arXiv:1106.0007)
Mack K. J., Wesley D. H., 2008, preprint (arXiv:0805.1531)
Madau P., Meiksin A., Rees M. J., 1997, ApJ, 475, 429
Meyer-Vernet N., 1985, Advances Space Res., 5, 37
Meys R. P., 1978, IEEE Trans. Microwave Theory Tech., 26, 34
Mirabel I. F., Dijkstra M., Laurent P., Loeb A., Pritchard J. R., 2011, A&A, 528, A149
Morandi A., Barkana R., 2011, preprint (arXiv:1102.2378)
Penfield P. J., 1962, IRE Trans. Circuit Theory, 9, 84
Peters W. M., Lazio T. J. W., Clarke T. E., Erickson W. C., Kassim N. E., 2011, A&A, 525, A128
Petrovic N., Oh S. P., 2011, MNRAS, 413, 2103
Pritchard J. R., Loeb A., 2008, Phys. Rev. D, 78, 103511
Pritchard J. R., Loeb A., 2010, Phys. Rev. D, 82, 023006
Pritchard J. R., Loeb A., Wyithe J. S. B., 2010, MNRAS, 408, 57
Robertson B. E., Ellis R. S., Dunlop J. S., McLure R. J., Stark D. P., 2010, Nat, 468, 49
Rogers A. E. E., Bowman J. D., 2008, AJ, 136, 641
Salisbury W. W., Fernald D. L., 1971, J. Astronautical Sci., 18, 236
Schleicher D. R. G., Banerjee R., Klessen R. S., 2009, ApJ, 692, 236
Sethi S. K., 2005, MNRAS, 363, 818
Shaver P. A., Windhorst R. A., Madau P., de Bruyn A. G., 1999, A&A, 345, 380
Stubbs T. J., Glenar D. A., Colaprete A., Richard D. T., 2010, Planet. Space Sci., 58, 830
Weinreb S., 1982, Electronics Division Internal Report 231, Noise Parameters of NRAO 1.5 GHz GASFET Amplifiers. National Radio Astronomical Observatory, Charlottesville, VA
Wild J. P., Smerd S. F., Weiss A. A., 1963, ARA&A, 1, 291
Wouthuysen S. A., 1952, AJ, 57, 31
Zarka P., 2004, in Beaulieu J., Lecavelier Des Etangs A., Terquem C., eds, ASP Conf. Ser. Vol. 321, Extrasolar Planets: Today and Tomorrow. Astron. Soc. Pac., San Francisco, p. 160

This paper has been typeset from a TEX/LATEX file prepared by the author.